HHS Public Access

Author manuscript

Analyst. Author manuscript; available in PMC 2018 March 27.

Published in final edited form as:

Analyst. 2017 March 27; 142(7): 1061–1072. doi:10.1039/c6an02603f.

Retinal oxidative stress at the onset of diabetes determined by synchrotron FTIR widefield imaging: Towards diabetes pathogenesis

Ebrahim Aboualizadeh[1], **Mahsa Ranji**[2], **Christine M. Sorenson**[3], **Reyhaneh Sepehr**[2], **Nader Sheibani**[4], and **Carol J. Hirschmugl**[1,*]

[1]Department of Physics, University of Wisconsin-Milwaukee, Milwaukee, USA

[2]Biophotonics Laboratory, University of Wisconsin-Milwaukee, Milwaukee, USA

[3]Department of Pediatrics, University of Wisconsin-Madison, Madison, USA

[4]Department of Ophthalmology and Visual Sciences, University of Wisconsin-Madison, Madison, USA

Abstract

Diabetic retinopathy is a microvascular complication of diabetes that can lead to blindness. In the present study, we aimed to determine the nature of diabetes-induced, highly localized biochemical changes in the neuroretina at the onset of diabetes. High-resolution synchrotron Fourier transform infrared (s-FTIR) wide field microscopy coupled with multivariate analysis (PCA-LDA) was employed to identify biomarkers of diabetic retinopathy with spatial resolution at the cellular level. We compared retinal tissue prepared from 6-week-old $Ins2^{Akita/+}$ heterozygous (Akita/+, N=6; a model of diabetes) male mice compared with the wild-type (control, N=6) mice. Male Akita/+ mice become diabetic at 4-weeks of age. Significant differences ($P<0.001$) in the presence of biomarkers associated with diabetes and segregation of spectra was achieved. Differentiating IR bands attributed to nucleic acids (964, 1051, 1087, 1226 and 1710 cm^{-1}), proteins (1662, 1608 cm^{-1}) and fatty acids (2854, 2923, 2956 and 3012 cm^{-1}) were observed between the Akita/+ and the WT samples. Comparison between distinctive layers of the retina, namely the photoreceptor retinal layer (PRL), outer plexiform layer (OPL), inner nuclear layer (INL) and inner plexiform layer (IPL) suggested that the photoreceptor layer is the most susceptible layer to the oxidative stress in short-term diabetes. Spatially-resolved chemical images indicated heterogeneities and oxidative-stress induced alterations in the diabetic retina tissue morphology compared with WT retina. In this study, the spectral biomarkers and the spatial biochemical alterations in the diabetic retina and in specific layers were identified for the first time. We believe that the conclusions drawn from these studies will help to bridge the gap in our understanding of the molecular and cellular mechanism that contribute to pathobiology of diabetic retinopathy.

Graphical abstract

[*]**Corresponding author:** Carol J Hirschmugl, PhD, Physics Department, College of Letters and Science, University of Wisconsin-Milwaukee, 3135 North Maryland Ave., Milwaukee, WI 53211, USA, Phone: +1-414-229-5748, cjhirsch@uwm.edu.

Competing financial interest

The authors declare no competing financial interests.

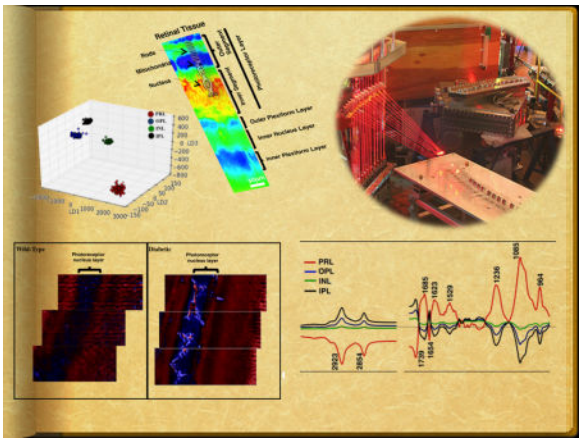

Keywords

synchrotron; FTIR imaging; spectroscopy; diabetes; oxidative stress; diabetic retinopathy; photoreceptor

1. Introduction

Diabetic retinopathy (DR), a progressive disease affecting the integrity and function of retinal circulation, is the leading cause of blindness in adults[1]. Development of DR can stimulate the growth of scar tissue and elevate the intraocular pressure. It is well established that neurovascular retinal changes occur during diabetes[2]. However, the biochemical nature of these changes and their consequences on retinal function remain largely unknown. It has been acknowledged that oxidative stress and pro-inflammatory changes make significant contribution to the pathogenesis of DR in animal models[3]. Reactive oxygen species (ROS) are constantly produced during normal oxidative metabolism and are removed by scavenging system; however, inefficient removal of ROS leads to excessive ROS and increased oxidative stress. Diabetes results in elevated oxidative stress that mainly damages to biological macromolecules[4]. However, mechanisms behind the contribution of oxidative stress to the development of diabetes still remain a challenge. Retina is the most susceptible tissue to the oxidative stress due to the higher content of polyunsaturated fatty acids (PUFAs). Membrane lipid peroxidation and oxidative damage to DNA are known as the consequences of increased level of ROS and superoxide in the diabetic retina[5,6].

Although DR is a slow progressing disease, it has been shown in animal models that in the initial stages (before any histopathological signs appear), the basement membrane of the capillaries is thickened[7]. Diabetes affects neuronal cells in the retina, which causes visual dysfunction and degeneration of some neurons. Recently, the impacts of DR on neuronal units of retina and the biochemical alterations including oxidative stress, apoptosis of neurons, and activation of microglial cells have been reported[8]. During diabetes, apoptosis of neurons occurs earlier than vascular cell apoptosis. It is critical to localize diabetes-induced damage and determine the origin of neurons that experience apoptosis. Therefore,

we aimed to determine the underlying biochemical changes in the neuroretina at early stages of diabetes.

Biological and biomedical applications of FTIR spectromicroscopy with the goal of classification, pattern recognition and pathology are highly sought after[9–13]. FTIR spectromicroscopy has been widely used in studying the pathology of various diseases including brain tumors[14], adenocarcinoma[15,16], prostate and breast cancer[17–21], lung cancer[22], lymph node[23], squamous cervical epithelium[24], or the biochemistry of neurons[25–27], antral oocytes[28] and stem cells[29]. Vibrational spectroscopic methods have been used in several studies to understand the diabetes-induced biochemical alterations in the kidney plasma membrane[30], liver microsomal membrane and soleus skeletal muscle[31], myocardia and vessels of the rat heart[32], human lips[33], and human saliva[34]. Thus, the use of appropriate imaging techniques to characterize biomolecular alterations attributed to DR is essential.

The aim of this study was to gain a deeper insight into the biochemical alterations in diabetic retina tissue by means of high-resolution chemically and spatially resolved FTIR images and chemometric tools. Chemical images from retinal tissue (flash-frozen samples) and the biochemistry of distinctive retinal layers have been previously studied[35]. In this article, diabetic (Akita/+) and wild-type (WT) retina tissues, which were imaged at the mid-infrared IRENI beamline at the Synchrotron Radiation Center (SRC), were studied for the first time to determine short-term diabetes-induced alterations in the retina tissue at subcellular levels for the first time. Principal component analysis followed by linear discriminant analysis (PCA-LDA) was performed to achieve the maximum classification between Akita/+ and WT retina tissues and reveal the spectral biomarkers attributed to the distinction between these tissues[36]. Here, for the first time, distinctive layers of retina were compared to detect highly localized diabetes-induced biochemical changes in the retina. Comparison between the retinal photoreceptor layer (PRL), outer plexiform layer (OPL), inner nuclear layer (INL) and inner plexiform layer (IPL) in this study suggested that photoreceptors are the primary target for oxidative stress during short-term diabetes.

2. Materials and Methods

2.1 Animals

All experiments were carried out in accordance with the Association for Research in Vision and Ophthalmology Statement for the Use of Animals in Ophthalmic and Vision Research and were approved by the Institutional Animal Care and Use Committee of the University of Wisconsin School of Medicine and Public Health. Male Akita/+ mice spontaneously develop diabetes at 4-weeks of age due to a mutation in their insulin gene. The Akita spontaneous mutation (commonly referred to as MODY; Maturity-Onset Diabetes of the Young) is an autosomal dominant mutation in the insulin II gene (Ins2) 22. Ins2 ^{Akita}-C57BL/6 diabetic mice develop retinal vascular pathology characteristic of the early stages of DR. Eyes were harvested from male WT and Akita/+ (all on C57BL/6 background) mice at 6-weeks of age. Eyes were immediately frozen in isopentane cooled to almost freezing in liquid nitrogen and later stored at −80 °C freezer for FTIR microspectroscopy. Freezing must be done quickly in

order to preserve the tissue integrity and avoid H_2O crystal formation in the tissue. Each group of samples contained 6 mice.

2.2 Retinal tissue preparation

Frozen eyes that were preserved at −80° C freezer were transported to the biotechnology facility (University of Wisconsin-Milwaukee) for sectioning using cryostat machine (Leica Model CM 3050S), which is designed for rapid sectioning of specimens. It was critical to assure that the temperature at which the tissue was cut (inside cryostat) was between −15 °C and −20 °C and the blade was pre-chilled for at least half an hour prior to sectioning. Eyes were embedded in optimal cutting medium (O.C.T) compound (Sakura Finetek Inc. USA) and an embedded eye was left inside the cryostat machine (at −20°C) for a minute (until the O.C.T will freeze and turn into a solid white color) prior to sectioning. Only small amount of O.C.T was applied to prevent tissue contamination. Eyes were dissected starting from the optic nerve (from back of the eye) and retinas were extracted using a thin paintbrush. The position of the eye was adjusted to be near the blade and the appropriate thickness was chosen (5–8 μm for FTIR measurements). At least, 5 retina sections were collected from each animal and the tissues were mounted on mid-IR BaF_2 window. The BaF_2 window was placed in a foil-wrapped cell suspension tube (visible-light exposure is not allowed) and preserved on dried ice for transporting to the laboratory for FTIR measurements. Prior to FTIR imaging, the samples were desiccated in dark, at the room temperature, and low humidity condition[37, 38]. The cryosections are light sensitive, therefore exposure to visible light is only required during instrumental setup. Schematic of the methodology is shown in Figure 1.

2.3 Synchrotron FTIR widefield microscopy

Advantages of the synchrotron-based FTIR imaging of the biological tissues have been previously described in several studies[39–45]. Here, the samples were evaluated with a Bruker Vertex 70 IR spectrometer and a Bruker Hyperion 3000 IR Microscope equipped with a multi-beam synchrotron source at IRENI beamline[46,47]. The focal plane array (FPA) detector was a multielement detector (128 × 128 pixels) coupled with an interferometer for collecting hyperspectral data sets (x, y, Abs (λ)). The measurements were performed using a 74× Cassegrain microscope objective (numerical aperture 0.65) and a 15× condenser aperture (N.A 0.4). With this experimental geometry, the effective geometric pixel size at the sample plane was 0.54 × 0.54 μm^2 [46]. The data were collected using 128 co-added scans at 4 cm^{-1} spectral resolution. Data were acquired using OPUS 6.5 software (Bruker). FTIR measurements of retina sections were performed in a transmission mode. Background was measured from no sample area on BaF_2 window and the ratio of sample measurement to background was evaluated as an absorption spectrum. The FPA size for the measurements was set to 64×64 pixels; therefore, 4096 individual spectra in the mid-IR wavelength range 3800–900cm^{-1} (every pixel contains an IR spectrum) were collected per single tile measurement. To cover a larger area of the tissue, 9 adjacent tiles were measured by mapping across the section of retina.

2.4 Data Pre-processing

Resultant spectra from tissues were partially influenced by Mie scattering. It is known that the IR radiation can scatter from particles with diameters in the range of 2–20 μm, and this artefact distorts the absorption bands leading to misinterpretation of the spectra[48–50]. Although the dispersion artefact appears as a derivative shape in the spectral region close to the Amide I band, this phenomenon could influence other peaks in the biochemical-IR region, and leads to misinterpretation of the peaks and pathology. In this study, nearly 192,000 individual pixel spectra (6 animals; each retina tissue measurement ≈32000 spectra) from WT tissues (including all retinal layers) and the same number of spectra from Akita/+ tissues (including all retinal layers) were generated and preprocessed as follows. CO_2 peak at 2350 cm^{-1} was removed, and the spectral regions 900–1800 cm^{-1} and 2750–3050 cm^{-1} were used. This resulted in 624 data points for multivariate analysis. Pixel binning (2×2; average of 4 pixels) was applied. This was necessary to increase signal to noise ratio, and S/N in every spectrum was then systematically evaluated using an in-house written code in Matlab. To remove Mie scattering effect and dispersion artefacts, RMieS-EMSC correction was applied to the data. The algorithm used for scattering correction in this work was implemented using Graphics Processing Units (GPUs) for fast hyperspectral processing and described elsewhere[52,53]. All spectra were vector-normalized using Matlab prior to computational analysis.

2.5 Computational and statistical analysis

In this study, Multivariate analysis PCA-LDA was performed (in-house written code in Python) to reveal the biomarkers and segregation between diabetic and control groups. Principal component analysis (PCA) is an unsupervised method to decompose a dataset into bilinear latent variables called principal components (PCs). This reduces the dimensionality of the data while retaining most of the information in the data set. PCA is calculated based on the maximum variance contained in the dataset in descending order of importance and there is a null correlation between components. The advantage of working with scores and loading representations is the reduced size of the big data and the efficacy to highlight and visualize the variations and heterogeneities in biological tissues. Linear discriminant analysis (LDA) is a supervised method to improve the segregation level and reveal clusters that are maximized based on the separation between multiple classes rather than variations within each group. Here PCA was used in the first stage and the optimum numbers of PCs were retained for subsequent LDA analysis (PCA-LDA), and cross-validated scores[54] were shown. The second piece of information originated from PCA-LDA analysis is the “cluster vector plot” that can be used for biomarker extraction. The cluster vector plots are used to infer the components and the strength of components that correspond to the observed biomarkers of the disease. The largest peaks or troughs in vector plots were associated with the most contributing feature to separation between classes[30]. Multivariate analysis was performed using “R” package (version 3.1.2), Matlab_R2016a and Python_2.6 version.

One-way-ANOVA statistical analysis was employed to determine whether there is any significant difference in the bands that are highlighted in both the WT and the Akita/+ samples. Results were studied as means ± standard deviations (S.D.) and P values, equal or

less than 0.05, were accepted as a significant level of difference between the groups. The statistical analysis was performed using SAS 8.0. software.

3. Results

The central premise of this study was designed to identify chemical signatures of retinal damage, and to gain a deeper insight into retinal biochemical changes associated with early stages of diabetese. This study was motivated by two specific aims: *i)* identifying and characterizing the biomarkers of mitochondrial oxidative damage and cellular lipids; and *ii)* understanding diabetes-induced alterations in biochemistry of distinctive retinal by means of spatially-resolved chemical images.

3.1 IR spectra and chemical images of retinas from WT and diabetic (Akita/+) mice

Absorption spectra of retina from Akita/+ mice compared with retinas from WT mice are demonstrated in the mid-IR spectral range (3600–900cm^{-1}) in Figure 2. There are subtle differences in the biochemical-fingerprint spectral region (1800–900 cm^{-1}) and unsaturated and saturated fatty acid regions (3050–2800cm^{-1}). Second derivative absorption spectra (Savitzky-Golay algorithm, 9 smoothing points) are shown in the spectral region 3050–2800 cm^{-1} associated with $\delta_{sym,asym}(CH_2, CH_3)$ and polyunsaturated fatty acids (PUFA) content, 1800–1470 cm^{-1} attributed to the secondary structure of proteins and 1470–900cm^{-1} mostly attributed to DNA/RNA bands. Absorption bands in the spectral region 1160–950 cm^{-1} are highly dominated by vibrations from C-O functional groups in carbohydrates, although ν_{symm} PO^{2-} modes also contributes at 1085 (±2) cm^{-1}. Figure 2, B–D demonstrates the peak wavenumber values for the important macromolecules of retinas from WT and Akita/+ mice, respectively. The band assignments are summarized in Table 1.

Chemical images demonstrated features of the mouse retina and its individual at subcellular level. Figure 3 depicts retina sections from WT and the Akita/+ mice. Figure 3A shows the photomicrograph of the retina oriented vertically from the choroid layer (the outermost layer of retina) to the ganglion cell layer, and the FTIR image are overlaid to visualize retinal layers with respect to the visible images. Figures 3B, C show the chemical images of the retina from WT and Akita/+ mice integrated underneath 1712 cm^{-1} peak (baselined region: 1725–1700cm^{-1}), and reveals the photoreceptor layer (PRL), the outer plexiform layer (OPL), inner nuclear layer (INL) and inner plexiform layer (IPL) within the retina. Chemical image of the retina from Akita/+ mice (Fig. 3C) is overlaid with the sketch of photoreceptor system including rod cells, mitochondria, and nucleus. Processed images of the retinal tissue at different frequencies and absorption spectra for the retina are discussed elsewhere[35]. In Figure 3 (red-blue color scale), regions of the highest absorption strength e.g. photoreceptor nucleus layer appeared red and the retinal layers with the lowest absorption strength were blue/purple. The same color scale was used for demonstration of both mosaics in each tissue. The H&E stained (after FTIR measurements) section of retina that highlights the nucleus segment of the photoreceptor layer has been shown elsewhere[35]. The outer segment of photoreceptors are mostly comprised of rod cells and are rich in PUFA content, while the rod inner segments are rich in mitochondria and Golgi apparatus. Comparison between photoreceptor nucleus layers in both tissues revealed decreased concentration of DNA and

more heterogeneity in retinas from Akita/+ mice compared with WT mice. As discussed previously[35], the outer and inner plexiform layers are rich in symmetric and asymmetric stretching of CH_2 and CH_3 functional groups, and the nucleus segment in photoreceptors (ONL) has very similar spectrum to INL. Chemical images in Figure 3 demonstrate the area of 128 × 270 μm^2 of the retinas from the Akita/+ and WT mice.

3.2 Wild-type *vs.* Akita/+ retinal tissue

Retinal tissues prepared from WT and Akita/+ mice were compared. IR absorption spectra generated from each pixel within hyperspectral image in the biochemical spectral region (1800–900 cm^{-1}) and the spectral region primarily attributed to lipids (3050–2750cm^{-1}) were pre-processed for loading into "PCA-LDA" analysis. Spectra from the whole retinal tissue covering the PRL, the OPL, the INL and the IPL were used for comparison. PC "scores" and "loadings" were generated principally from PCA analysis to identify the class segregation and the wavenumbers responsible for the segregation of clusters. LDA was then performed to maximize the variance between groups rather than variations within each group. Figure 4A shows 1-dimensional cross-validated scores plot of the retina from WT *vs.* Akita/+ mice after PCA-LDA analysis and the classification. Figure 4B depicts the "cluster vector plot" generated from the loadings and discriminating wavenumbers responsible for the separation between the retinas from diabetic and non-diabetic mice. Major differentiating bands that lie in the biochemical spectral region were 1739 cm^{-1}, 1710 cm^{-1}, 1662 cm^{-1}, 1608 cm^{-1}, 1550 cm^{-1}, 1226 cm^{-1} and 1151 cm^{-1}. While other important bands were observed at 964 cm^{-1}, 987 cm^{-1}, 1051 cm^{-1}, 1085 cm^{-1} and 1488 cm^{-1} (lipids). Discriminative bands in the spectral region, associated with saturated and unsaturated fatty acids region, were 2854 cm^{-1}, 2923 cm^{-1}, 2956 cm^{-1}, and an olefinic band at 3012 cm^{-1}. The list of differentiating bands between WT and Akita/+ tissues and their biomolecular assignments are summarized in Table 2.

3.3 Photoreceptor layer *vs.* Inner and Outer plexiform layers *vs.* Inner nuclear layer

To gain a better understanding of the impact of oxidative stress on distinctive retinal layers, a separate comparison was made between the PRL, OPL, INL and IPL in the retinal tissue from Akita/+ mice. Individual pixel IR spectra were derived from characteristic layers and compared by using PCA-LDA analysis. Figure 5A shows 3D scores plot where there was a separation between the PRL and the rest of the retinal layers along LD1. Along LD2, the IPL separated from OPL and INL, while there is some overlap between PRL and IPL. LD3 separated the OPL from IPL and INL with higher degrees of overlap compared with LD2, and still overlaps with PRL. 3D scores plot revealed the separation of PRL compared with other retinal layers, and there was more variation within the PRL scores compared with the tightly clustered scores in the other layers. Figure 5B demonstrates the cluster vector plot for all retinal layers, and when the PRL scores were compared to the scores of OPL, INL and IPL (Figure 5-A), the most notable contributing peaks in the loading plot between 1800 and 900 cm^{-1} were 1739 cm^{-1}, 1685 cm^{-1}, 1654 cm^{-1}, 1623 cm^{-1}, 1529 $cm^{-}1$, 1236 cm^{-1}, 1085 cm^{-1}, and 964 cm^{-1}, respectively. The major contributing bands between the PRL and rest of the layers in the lipid region were 2850 cm^{-1} and 2921 cm^{-1}. The largest peaks in biochemical-IR region, responsible for segregating between the PRL and the other layers

were attributed to nucleic acids. The list of differentiating wavenumbers between the PRL and the other layers with their biomolecular assignments are summarized in Table 3.

3.4 Nucleic acid to protein ratio in the retinal tissue

To reinforce the rationality of our findings and obtain a better knowledge of diabetes-induced alterations in the composition and concentration of molecules, the band area ratios for some functional groups of retinal tissues from WT and Akita/+ mice were evaluated. In tissue studies, the differences in the thickness of tissues can influence cellular alterations and spectral interpretation. Thus, to avoid such errors the ratio of integral intensities was employed. ν_{asym} PO^{2-} to protein ratio was calculated by dividing the baseline-corrected area under the functional group attributed to asymmetric stretching of phosphates at 1230 cm^{-1} and one of the main FTIR markers of DNA[60, 61] by Amide II absorption band (1544 cm^{-1}). The ratio was calculated for the PRL, OPL, INL and IPL of the retina in both types of mice, and a comparison was made of the layers per tissue type (WT *vs.* Akita/+) and per layer for each tissue. The spectral regions 1180–1280 cm^{-1} (for the phosphate band) and 1500–1750 cm^{-1} (for Amide II band) were used as a baseline. The PRL demonstrated the highest amount of ν_{asym} PO^{2-}/protein (in both tissues) compared to OPL, INL and IPL. The sample from Akita/+ mice had a higher amount of this ratio in all layers compared to WT group. Both tissues follow the same trend of having either increasing or decreasing ν_{asym} PO^{2-}/protein between layers. P-values were calculated and $P < 0.05$ was considered to be significantly different among groups of samples and retina layers. Results from the statistical analysis for both tissues are demonstrated in Figure 6A. A spectral map of ν_{asym} PO^{2-} to protein ratio of retinas from WT and Akita/+ mice are shown in Figures 6B, C. These ratio images were used to visually discern the strength of the relative concentration of phosphates and alterations in tissue morphology associated with diabetes-induced damage between the layers. The area of nearly 270 × 270 μm^2 of the retina tissues are shown in Figures 6B, C, where the blue color shows the highest value of ratio and the red color indicates the lowest value. This Figure demonstrates the strength of PRL and in particular the nuclear segment of the photoreceptor layer compared to the other layers. The ratio image for the retina from WT mice shows a homogenous morphology within the retinal layers, while the retina from Akita/+ mice were more heterogeneous in the nuclear segment of photoreceptors. The ν_{asym} PO^{2-} to protein ratio images (Fig. 6) enabled us to resolve in detail the subtle heterogeneities observed in the inner segment of photoreceptors within chemical images of diabetic retina (Fig. 3C).

3.5 Unsaturation level and hydrocarbon acyl chains in lipids

The olefinic to lipid ratio, also known as unsaturation index, is used to find the relative amount of unsaturated lipids in retinal tissue. This ratio is calculated by dividing the area of the ν=(CH) peak at 3012 cm^{-1}, attributed mainly to unsaturated lipids, by area of the C-H region attributed to symmetric and asymmetric stretching of CH_2 and CH_3 in 2830–2980 cm^{-1} (lipids). The spectral region 2800–3050 cm^{-1} was used as a baseline region. A remarkable decrease in the ratio was observed in retinal layers from Akita/+ mice compared with WT mice, while the PRL demonstrated the largest decrease amongst the layers (Figure 7A).

To determine the diabetes-induced changes in hydrocarbon acyl chain length of lipids, the ratio of ν_{as} CH_2/ν_{as} CH_3 was calculated. There was an increase in retinal layers from Akita/+ mice compared with WT mice (Figure 7B). As shown in Table 1, the areas under 2960 cm^{-1} and 2921 cm^{-1} bands were calculated and there was an increase in the band area in Akita/+ groups (for all retinal layers) compared with WT groups. The variation of ratio between WT layers was negligibly smaller. The results of statistical analysis are shown in Figure 7B.

4. Discussion

Understanding biophysical and biochemical features of retinal tissue at subcellular level plays a major role in the pathogenesis of diabetes and particularly, in revealing the mechanism underlying the oxidative stress damage in the retina. Identifying biomarkers with spatial resolution at the cellular and molecular level is critical for early detection and a better understanding of the disease pathogenesis. The first goal of this study, which was the determination of biomarkers of diabetes-induced oxidative damage in the retina, was achieved by employing PCA-LDA. We demonstrated the efficacy of s-FTIR imaging and multivariate image analysis in classification of control and diabetic tissues (Fig. 4) and the series of IR bands (Table 2) in proteins, nucleic acids, and lipids attributed to this separation were found. FTIR images of retinas that were imaged at the most advanced infrared beamline (IRENI) revealed all distinctive layers of the retina. High resolution spatially resolved chemical images integrated over the IR band at 1712 cm^{-1} from Akita/+ tissue demonstrated heterogeneous morphology within the nucleus segment of photoreceptors, while the WT retina tissue looked more homogenous within the same layer (Fig. 3C). However, the OPL, INL, and IPL revealed a homogenous structure in both WT and Akita/+ tissues. Notably, the band at 1712 cm^{-1} has been only observed in the spectra from the nucleus segment of photoreceptors[35]. The 1712 cm^{-1} band has also been reported as a marker for determination of free fatty acids[62], and carbonyl group products that are produced by deposition of glycation products[63]. This band was found as one of the major differentiating wavenumbers between the WT and Akita/+ tissues, which suggests the significance of the photoreceptor cell's nucleus in the observed classification.

The second goal of this study was to determine the diabetes-induced alterations in the biochemistry of distinctive layers of the retina. Three-dimensional scores plot from PCA-LDA analysis exclusively on Akita/+ tissue (Fig. 5A) revealed clear separation among the retinal layers. Along LD1, there was a separation between PRL and the rest of the layers, and the IR bands that were responsible for the classification are reported (Table 3). This finding recommended that at the initial stage of DR, PRL was the most vulnerable retinal layer in comparison with the other layers. There were three major differentiating bands in the DNA/RNA region (1425–900 cm^{-1}) of the cluster vector plot at 964cm^{-1} (symmetric PO_4^- stretching (DNA)/deoxyribose/backbone (C-C)), 1085cm^{-1} (ν_{sym} PO^{2-}), and 1236 cm^{-1} (ν_{asym} PO^{2-}) (Fig. 5B). Peak characteristic for symmetric and asymmetric phosphate bands at 1080 and 1236 cm^{-1}, for the inner and outer segments of photoreceptor has been shown[35]. The peaks of symmetric and asymmetric stretching vibrations of phosphates have been reported in the double stranded DNA spectra in several studies[60,61]. The ratio of ν_{asym} PO^{2-} to protein was also found (Fig. 6) to provide information about the changes in nucleic

acid content in comparison with protein content. The higher level of ν_{asym} PO^{2-}/protein in the PRL in our findings could be indicative of localization of DNA damage in PRL, due to the proximity of nuclei to sites of superoxide generation in photoreceptors. Heterogeneities in the ratio images of retinas from Akita/+ mice that appeared within nucleus segment of PRL (Figure 6C) suggest morphological changes as a result of diabetes-induced oxidative stress. The morphological variations in the thickness of retinal layers at different stages of diabetes, and the role of early phase photoreceptor loss during diabetes have been studied[64]. We believe that the segregation between PRL (which is a dense layer in nuclei) and the other layers, and the presence of differentiating bands attributed to nucleic acids, indicates the oxidative DNA damage in the retina, and in particular in the PRL.

It is well established that the oxidative damage to DNA is elevated in the retina at early stages of diabetes mellitus[65–67]. The significance of photoreceptor changes in the pathogenesis of DR is evaluated in several studies[68–70]. Photoreceptors are the major source of superoxide and reactive oxygen species (ROS) compared with INL or ganglion cell layer (GCL) and contribute to the greater extent to the oxidative stress during diabetes[71]. Most of the mitochondria are located in the photoreceptor layer (where we observe the most variations between diabetic and WT tissues) and mitochondrial DNA (mtDNA) is the most vulnerable target for ROS and oxidative damage[72]. The contribution of mitochondria in diabetes-induced oxidative damage is well-established[73,74].

Our results also identified differentiating spectral features between WT and Akita/+ retina in saturated and unsaturated fatty acids (Fig. 4). The differentiating peak at 3012 cm^{-1} could be attributed to the richness of PUFA disks in the inner segment of photoreceptors. The olefinic to lipid ratio, used as the level of unsaturation in lipids, decreased in Akita/+ mice compared with WT mice. Notably, the diabetic PRL showed the largest decrease among the retinal layers (Fig. 7A). The decrease in this ratio in diabetic retinal layers, suggests the loss of unsaturation in acyl chains of lipids due to an elevated lipid peroxidation in diabetic retina. 4-Hydroxyalkenals are the most toxic products in lipid peroxidation and were found in the retina as early as 6 weeks of diabetes[75]. Our results was found to be in agreement with several studies on diabetes-induced changes in retinal fatty acid metabolism[76,77] that revealed a significant decrease in unsaturation level in diabetic retina. Lipid peroxidation serves as an indicator of the oxidative stress in diabetes mellitus[52], and it occurs due to the abundance of unsaturated fatty acids in biological membranes that are mainly attacked by free radicals. The oxidation of unsaturated fatty acids is well established and poly-unsaturated fatty acids are more susceptible to peroxidation due to the number of double bonds[78]. The changes in unsaturated fatty acids can affect the structure and functionality of the membranes and signal propagation; however, these changes can adversely affect the integrity of membrane[79].

CH_2/CH_3 antisymmetric stretching ratio (FTIR-based hydrocarbon acyl chain in lipids) was larger for Akita/+ mice compared with WT mice, and it was significantly larger for OPL and IPL due to the richness of the plexiform layers in lipids associated with the network of axons and synapses (Fig. 7B). The IPL and OPL demonstrated comparable biochemistry in the chemical images integrated at peaks 2850 cm^{-1} and 1738 cm^{-1}, shown in ref[35]. Qualitative longer chains of hydrocarbon acyl of lipids in diabetic groups suggest changes in the

membrane and lipid metabolism[80] at the early stages of diabetes, and the significance of plexiform layers in these alterations compared to the outer and inner nucleus segments of the retina.

5. Conclusion

DR causes progressive damage to the retina tissue that can lead to serious complications including retinal detachment, vitreous hemorrhage, glaucoma, and blindness. Here we demonstrated the efficacy of high-resolution synchrotron-based FTIR wide field imaging and PCA-LDA to differentiate between diabetic and control retina tissues with robust classification, and determine the highly localized early diabetes-induced biochemical alterations in the retina. Spectral biomarkers of diabetes-induced changes in distinctive retinal layers attributed to nucleic acids, proteins, and lipids, were delineated. This is the first study to report the nature of molecular changes in the biochemistry of distinctive layers of retina during diabetes. One important finding of this study is that super resolution FTIR images providing information about the significance of PRL at the onset of DR and the heterogeneities associated with diabetes-induced changes in the nucleus segment of photoreceptors. Findings from ratios of several IR bands, including an increase in nucleic acid/protein, a decrease in olefinic/lipid, and an increase in hydrocarbon acyl chains in lipids, in the diabetic retina, is reported. Comparison between distinctive layers of retina in the diabetic and WT mice indicated that the PRL experienced the most obvious impact at the onset of diabetes. The current study provides substantial mechanistic understanding of the oxidative damage in the retina, which may shed import insight into the pathogenesis and diagnosis of DR. Future work will focus on temporal and persistence of these changes and their contribution to retinal complications associated with diabetes.

Acknowledgments

This work was supported in part by the National Institutes of Health Grants EY022883 and P30 EY016665, Environmental Protection Agency 83573701, NSF grants CHE-1508240 and CHE-1112433, and an unrestricted award to the Department of Ophthalmology and Visual Sciences from Research to Prevent Blindness. NS is a recipient of Alice R. McPherson-Retina Research Foundation Chair. CMS is a recipient of Retina Research Foundation Daniel M. Albert Chair.

Abbreviations

DR	Diabetic Retinopathy
WT	Wild Type
PRL	Photoreceptor retinal layer
OPL	Outer plexiform layer
INL	Inner nucleus layer
IPL	Inner plexiform layer
PUFA	Poly-unsaturated fatty acid
PCA	Principal component analysis

LDA Linear discriminant analysis

References

1. Prasad S, Kamath GG, Jones K, Clearkin LG, Phillips RP. Eye. 2001; 15:640–643. [PubMed: 11702977]
2. Ly A, Yee P, Vessey KA, Phipps JA, Jobling AI, Fletcher EL. Investigative Ophthalmology & Visual Science. 2011; 52:9316–9326. [PubMed: 22110070]
3. Kowluru RA, Chan PS. Experimental Diabetes Research. 2007; 2007:43603–43615. [PubMed: 17641741]
4. Maritim AC, Sanders RA, Watkins JB. Journal of Biochemical and Molecular Toxicology. 2003; 17:24–38. [PubMed: 12616644]
5. Kowluru RA. Acta Diabetologica. 2001; 38:179–185. [PubMed: 11855796]
6. Kowluru RA, Abbas SN. Investigative Ophthalmology & Visual Science. 2003; 44:5327–5334. [PubMed: 14638734]
7. Roy S, Ha J, Trudeau K, Beglova E. Current Eye Research. 2010; 35:1045–1056. [PubMed: 20929292]
8. Stem MS, Gardner TW. Current Medicinal Chemistry. 2013; 20:3241–3250. [PubMed: 23745549]
9. Mattson EC, Aboualizadeh E, Barabas ME, Stucky CL, Hirschmugl CJ. International Journal of Molecular Sciences. 2013; 14:22753–22781. [PubMed: 24256815]
10. Chan KLA, Kazarian SG. Chemical Society Reviews. 2016; 45:1850–1864. [PubMed: 26488803]
11. Walsh MJ, Reddy RK, Bhargava R. Ieee Journal of Selected Topics in Quantum Electronics. 2012; 18:1502–1513.
12. Kazarian SG, Chan KLA. Biochimica Et Biophysica Acta-Biomembranes. 2006; 1758:858–867.
13. Bellisola G, Sorio C. American Journal of Cancer Research. 2012; 2:1–21. [PubMed: 22206042]
14. Bambery KR, Schultke E, Wood BR, MacDonald STR, Ataelmannan K, Griebel RW, Juurlink BHJ, McNaughton D. Biochimica Et Biophysica Acta-Biomembranes. 2006; 1758:900–907.
15. Lasch P, Haensch W, Naumann D, Diem M. Biochimica Et Biophysica Acta-Molecular Basis of Disease. 2004; 1688:176–186.
16. Quaroni L, Casson AG. Analyst. 2009; 134:1240–1246. [PubMed: 19475154]
17. Gazi E, Dwyer J, Gardner P, Ghanbari-Siahkali A, Wade AP, Miyan J, Lockyer NP, Vickerman JC, Clarke NW, Shanks JH, Scott LJ, Hart CA, Brown M. Journal of Pathology. 2003; 201:99–108. [PubMed: 12950022]
18. Levin IW, Bhargava R. Annual Review of Physical Chemistry. 2005; 56:429–474.
19. Fernandez DC, Bhargava R, Hewitt SM, Levin IW. Nature Biotechnology. 2005; 23:469–474.
20. Gasper R, Mijatovic T, Benard A, Derenne A, Kiss R, Goormaghtigh E. Biochimica Et Biophysica Acta-Molecular Basis of Disease. 2010; 1802:1087–1094.
21. Malins DC, Johnson PM, Barker EA, Polissar NL, Wheeler TM, Anderson KM. Proceedings of the National Academy of Sciences of the United States of America. 2003; 100:5401–5406. [PubMed: 12702759]
22. Yano K, Ohoshima S, Gotou Y, Kumaido K, Moriguchi T, Katayama H. Analytical Biochemistry. 2000; 287:218–225. [PubMed: 11112267]
23. Bird B, Miljkovic M, Romeo MJ, Smith J, Stone N, George MW, Diem M. BMC clinical pathology. 2008; 8
24. Wood BR, Chiriboga L, Yee H, Quinn MA, McNaughton D, Diem M. Gynecologic Oncology. 2004; 93:59–68. [PubMed: 15047215]
25. Barabas ME, Mattson EC, Aboualizadeh E, Hirschmugl CJ, Stucky CL. Journal of Biological Chemistry. 2014; 289:34241–34249. [PubMed: 25271163]
26. Hackett MJ, Borondics F, Brown D, Hirschmugl C, Smith SE, Paterson PG, Nichol H, Pickering IJ, George GN. Acs Chemical Neuroscience. 2013; 4:1071–1080. [PubMed: 23638613]
27. Hackett MJ, Caine S, Liu X, May TE, Borondics F. Vibrational Spectroscopy. 2015; 77:51–59.

28. Ami D, Mereghetti P, Natalello A, Doglia SM, Zanoni M, Redi CA, Monti M. Biochimica Et Biophysica Acta-Molecular Cell Research. 2011; 1813:1220–1229.
29. Kelly JG, Nakamura T, Kinoshita S, Fullwood NJ, Martin FL. Analyst. 2010; 135:3120–3125. [PubMed: 20886154]
30. Bozkurt O, Severcan M, Severcan F. Analyst. 2010; 135:3110–3119. [PubMed: 20967384]
31. Severcan F, Bozkurt O, Gurbanov R, Gorgulu G. Journal of Biophotonics. 2010; 3:621–631. [PubMed: 20575104]
32. Toyran N, Lasch P, Naumann D, Turan B, Severcan F. Biochemical Journal. 2006; 397:427–436. [PubMed: 16719841]
33. Yoshida S, Yoshida M, Yamamoto M, Takeda J. Journal of Pharmaceutical and Biomedical Analysis. 2013; 76:169–176. [PubMed: 23333685]
34. Scott DA, Renaud DE, Krishnasamy S, Meric P, Buduneli N, Cetinkalp S, Liu KZ. Diabetology & Metabolic Syndrome. 2010; 2
35. Kastyak-Ibrahim MZ, Nasse MJ, Rak M, Hirschmugl C, Del Bigio MR, Albensi BC, Gough KM. Neuroimage. 2012; 60:376–383. [PubMed: 22197789]
36. Martin FL, German MJ, Wit E, Fearn T, Ragavan N, Pollock HM. Journal of Computational Biology. 2007; 14:1176–1184. [PubMed: 17990977]
37. Baker MJ, Trevisan J, Bassan P, Bhargava R, Butler HJ, Dorling KM, Fielden PR, Fogarty SW, Fullwood NJ, Heys KA, Hughes C, Lasch P, Martin-Hirsch PL, Obinaju B, Sockalingum GD, Sule-Suso J, Strong RJ, Walsh MJ, Wood BR, Gardner P, Martin FL. Nature Protocols. 2014; 9:1771–1791. [PubMed: 24992094]
38. Stitt DM, Kastyak-Ibrahim MZ, Liao CR, Morrison J, Albensi BC, Gough KM. Vibrational Spectroscopy. 2012; 60:16–22.
39. Miller LM, Dumas P. Biochimica Et Biophysica Acta-Biomembranes. 2006; 1758:846–857.
40. Marcelli A, Cricenti A, Kwiatek WM, Petibois C. Biotechnology Advances. 2012; 30:1390–1404. [PubMed: 22401782]
41. Dumas P, Sockalingum GD, Sulé-Suso J. Trends in biotechnology. 2006; 25:40–44. [PubMed: 17116340]
42. Miller, L., Tobin, MJ., Srichan, S., Dumas, P. Biomedical Applications of FTIR Spectroscopy. 2nd. Barth, A., Haris, P., editors. IOS Press; Netherlands: 2008. p. 403-428.Ch. 14
43. Mattson, EC., Unger, M., Sedlmair, J., Nasse, M., Aboualizadeh, E., Alavi, Z., Hirschmugl, CJ. Infrared and Raman Spectroscopic Imaging. 2nd. Salzer, R., Siesler, HW., editors. Wiley-VCH Verlag GmbH & Co. KGaA; USA: 2014. p. 585-618.Ch. 15
44. Holman HYN, Bechtel HA, Hao Z, Martin MC. Analytical Chemistry. 2010; 82:8757–8765. [PubMed: 20839782]
45. Holman HYN, Bjornstad KA, McNamara MP, Martin MC, McKinney WR, Blakely EA. Journal of Biomedical Optics. 2002; 7:417–424. [PubMed: 12175292]
46. Nasse MJ, Walsh MJ, Mattson EC, Reininger R, Kajdacsy-Balla A, Macias V, Bhargava R, Hirschmugl CJ. Nature Methods. 2011; 8:413–U458. [PubMed: 21423192]
47. Hirschmugl CJ, Gough KM. Applied Spectroscopy. 2012; 66:475–491. [PubMed: 22524953]
48. Davis BJ, Carney PS, Bhargava R. Analytical Chemistry. 2010; 82:3487–3499. [PubMed: 20392064]
49. Davis BJ, Carney PS, Bhargava R. Analytical Chemistry. 2010; 82:3474–3486. [PubMed: 20392063]
50. Bassan P, Kohler A, Martens H, Lee J, Byrne HJ, Dumas P, Gazi E, Brown M, Clarke N, Gardner P. Analyst. 2010; 135:268–277. [PubMed: 20098758]
52. Mattson EC, Unger M, Clede S, Lambert F, Policar C, Imtiaz A, D'Souza R, Hirschmugl CJ. Analyst. 2013; 138:5610–5618. [PubMed: 23826609]
53. Imtiaz, A. Master of Science thesis. University of Wisconsin-Milwaukee; 2015. Scattering Correction Methods of Infrared Spectra Using Graphics Processing Units.
54. Baker MJ, Gazi E, Brown MD, Shanks JH, Gardner P, Clarke NW. British Journal of Cancer. 2008; 99:1859–1866. [PubMed: 18985044]
55. Barth A, Zscherp C. Quarterly Reviews of Biophysics. 2002; 35:369–430. [PubMed: 12621861]

56. Naumann D. Applied Spectroscopy Reviews. 2001; 36:239–298.
57. Movasaghi Z, Rehman S, Rehman IU. Applied Spectroscopy Reviews. 2008; 43:134–179.
58. Meade AD, Lyng FM, Knief P, Byrne HJ. Analytical and Bioanalytical Chemistry. 2007; 387:1717–1728. [PubMed: 17102969]
59. Liu KZ, Jackson M, Sowa MG, Ju HS, Dixon IMC, Mantsch HH. Biochimica Et Biophysica Acta-Molecular Basis of Disease. 1996; 1315:73–77.
60. Banyay M, Sarkar M, Graslund A. Biophysical Chemistry. 2003; 104:477–488. [PubMed: 12878315]
61. Whelan DR, Bambery KR, Heraud P, Tobin MJ, Diem M, McNaughton D, Wood BR. Nucleic Acids Research. 2011; 39:5439–5448. [PubMed: 21447564]
62. Lam HS, Proctor A, Meullenet JF. Journal of the American Oil Chemists Society. 2001; 78:1271–1275.
63. Huang YT, Liao HF, Wang SL, Lin SY. Aims Biophysics. 2016; 3:247–260.
64. Park SH, Park JW, Park SJ, Kim KY, Chung JW, Chun MH, Oh SJ. Diabetologia. 2003; 46:1260–1268. [PubMed: 12898017]
65. Finkel T, Holbrook NJ. Nature. 2000; 408:239–247. [PubMed: 11089981]
66. Baynes JW, Thorpe SR. Diabetes. 1999; 48:1–9. [PubMed: 9892215]
67. Kowluru RA, Chan PS. Experimental Diabetes Research. 2007; 2007:43603–43615. [PubMed: 17641741]
68. Greenstein V, Sarter B, Hood D, Noble K, Carr R. Invest Ophthalmol Vis Sci. 1991; 31:1008–1014.
69. Holopigian K, Greenstein VC, Seiple W, Hood DC, Carr RE. Ophthalmol Vis Sci. 1997; 38:2355–2365.
70. Kern TS, Berkowitz BA. Journal of Diabetes Investigation. 2015; 6:371–380. [PubMed: 26221514]
71. Du Y, Veenstra A, Palczewski K, Kern TS. Proceedings of the National Academy of Sciences of the United States of America. 2013; 110:16586–16591. [PubMed: 24067647]
72. Ames BN, Shigenaga MK, Hagen TM. Proceedings of the National Academy of Sciences of the United States of America. 1993; 90:7915–7922. [PubMed: 8367443]
73. Du YP, Miller CM, Kern TS. Free Radical Biology and Medicine. 2003; 35:1491–1499. [PubMed: 14642397]
74. Nishikawa T, Edelstein D, Du XL, Yamagishi S, Matsumura T, Kaneda Y, Yorek MA, Beebe D, Oates PJ, Hammes HP, Giardino I, Brownlee M. Nature. 2000; 404:787–790. [PubMed: 10783895]
75. Baydas G, Tuzcu M, Yasar A, Baydas B. Acta Diabetologica. 2004; 41:123–128. [PubMed: 15666580]
76. Tikhonenko M, Lydic TA, Wang Y, Chen WQ, Opreanu M, Sochacki A, McSorley KM, Renis RL, Kern T, Jump DB, Reid GE, Busik JV. Diabetes. 2010; 59:219–227. [PubMed: 19875612]
77. Koehrer P, Saab S, Berdeaux O, Isaico R, Gregoire S, Cabaret S, Bron AM, Creuzot-Garcher CP, Bretillon L, Acar N. Plos One. 2014; 9
78. Halliwell B, Chirico S. American Journal of Clinical Nutrition. 1993; 57:715–725.
79. AH Lewis, RN., McElhaney, RN. The Structure of Biological Membranes. 3rd. Yeagle, PL., editor. CRC Press; New York: 2011. p. 29-36.ch. 4
80. Pamplona R. Biochimica Et Biophysica Acta-Bioenergetics. 2008; 1777:1249–1262.

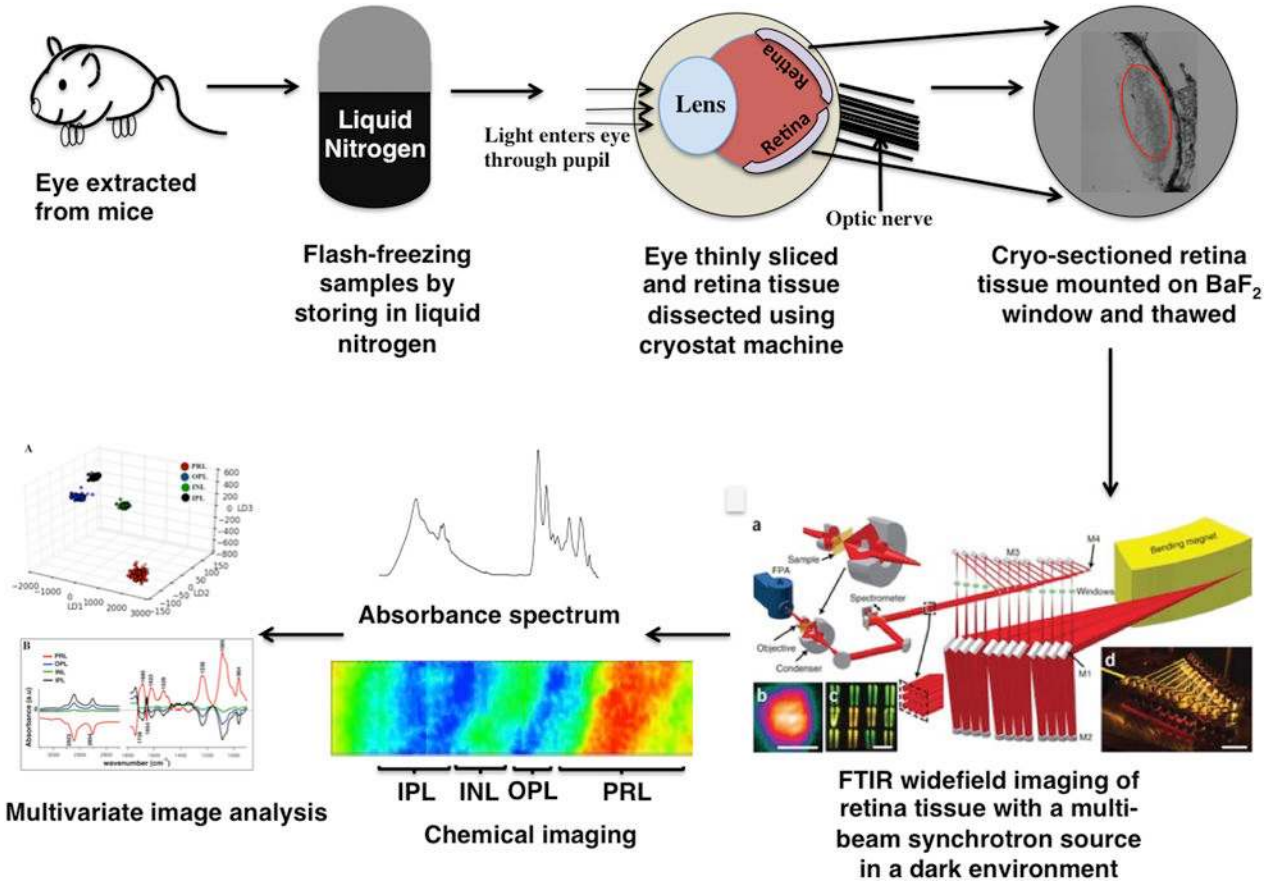

Figure 1.
schematics of the experimental design.

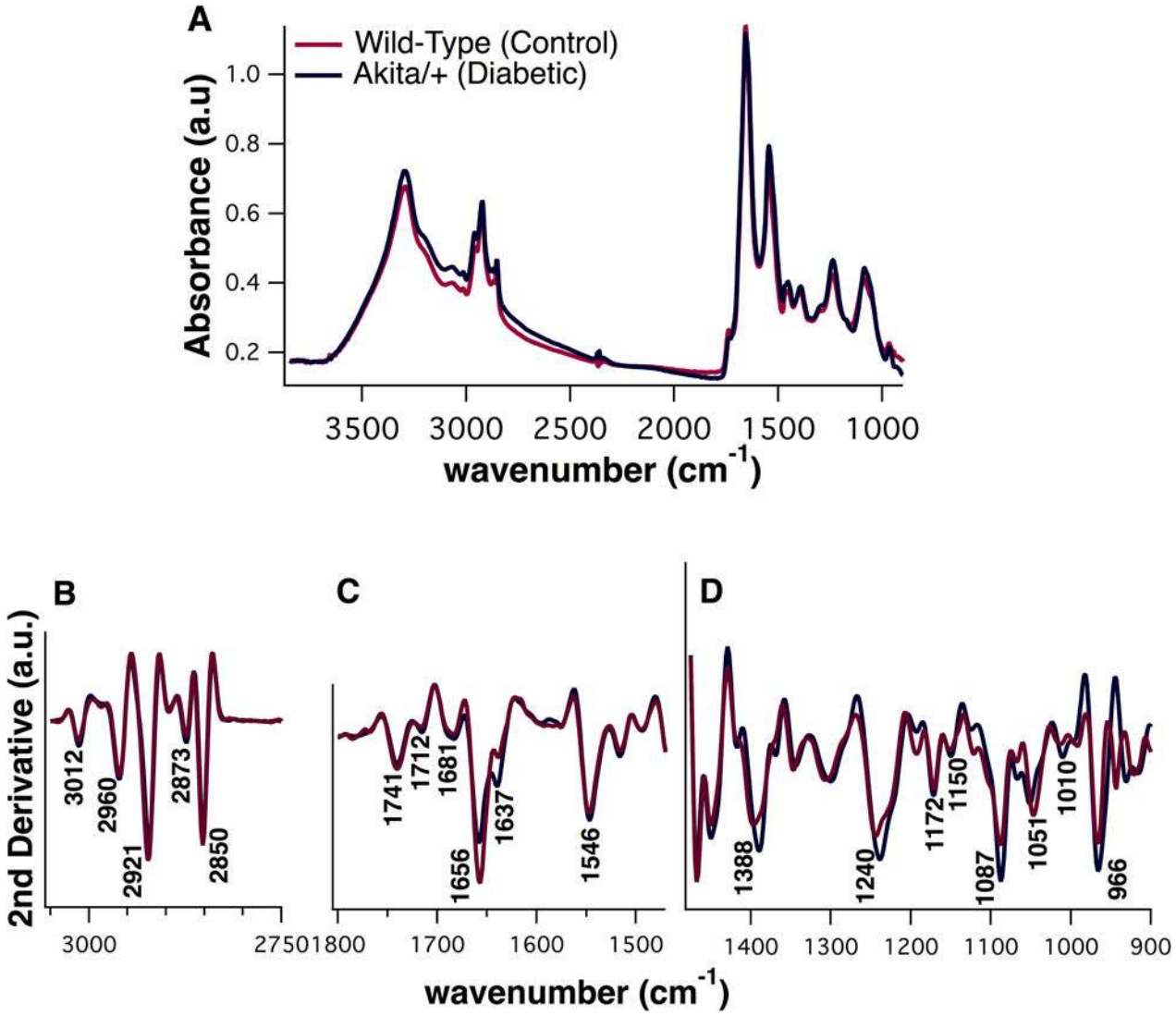

Figure 2.

ftir absorption spectrum analysis. a) average spectra of retina tissues from wild-type (wt) and akita/+ mice in the spectral range 3600–900cm^{-1} are shown. second derivative absorption spectra of the wt vs. akita/+ tissue is shown b) in the lipid region 3050–2750cm^{-1}, c) protein region 1800–1500cm^{-1} and d) dna/rna region 1425–900cm^{-1}. spectra were generated from the whole retina (including all retinal layers) and an average of 32,000 individual pixel spectra is demonstrated.

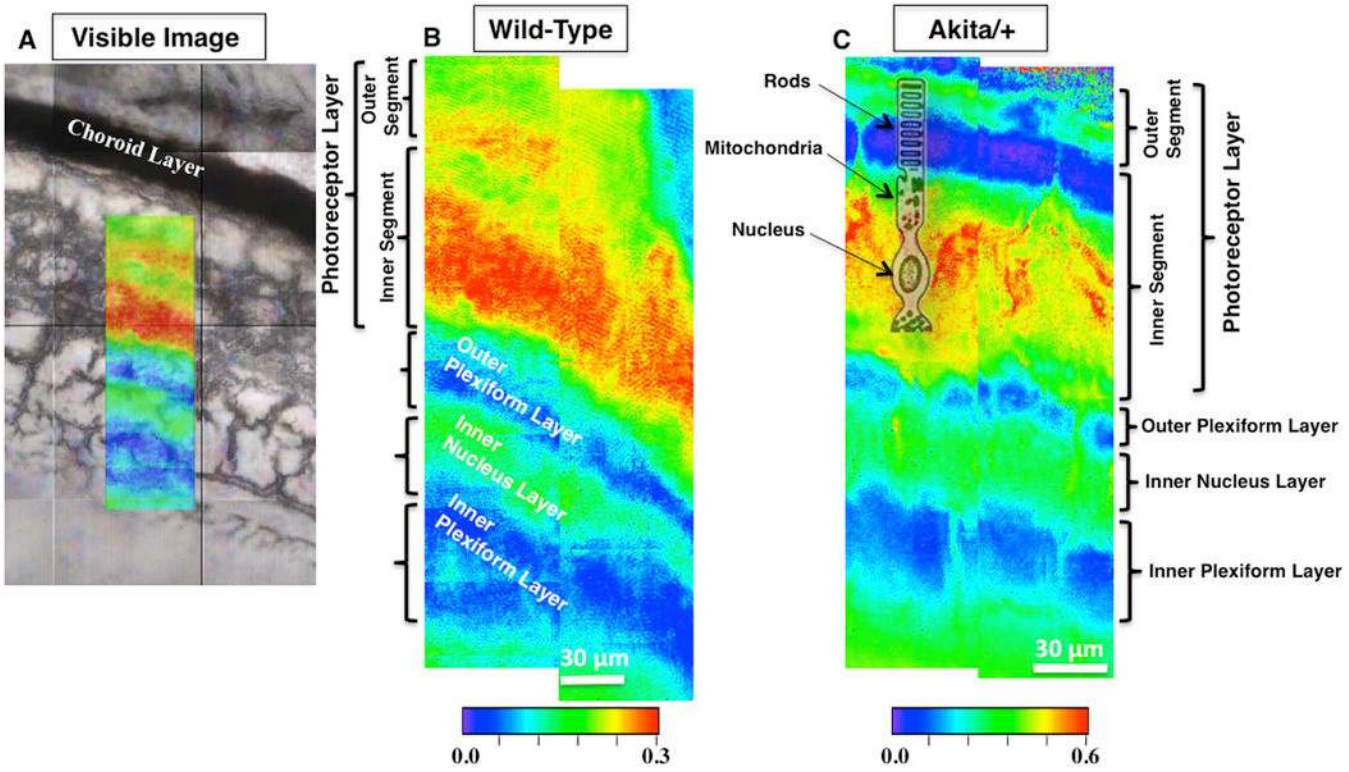

Figure 3.

a) photomicrograph of retinal tissue with an overlaid ftir image with localization of retinal layers. b, c) chemical images of the retina from wt and akita/+ mice highlighting distinctive layers of retina. each tissue covers the area of ≈128×270 µm2 (2 mosaics, 2 × 8 tiles (each tile = 64×64 pixels)), and integrated over the nucleic acid band at 1712 cm^{-1} (the linear baseline is set at 1700–1725 cm^{-1}) to highlight the absorption strength of this band in retinal layers. the inner, outer and nucleus segments of the photoreceptor system, opl, inl and ipl, are shown. panel c has been overlaid with the sketch of the photoreceptor system of retina including rods, mitochondria, and nucleus. scale bar is 30 µm and the color scale is from blue (the lowest absorption strength) to red (the highest absorption strength). the color scales 0–0.3 (wt) and 0–0.6 (akita/+) was used for this plot and the same colorscale was used for both mosaics in each tissue.

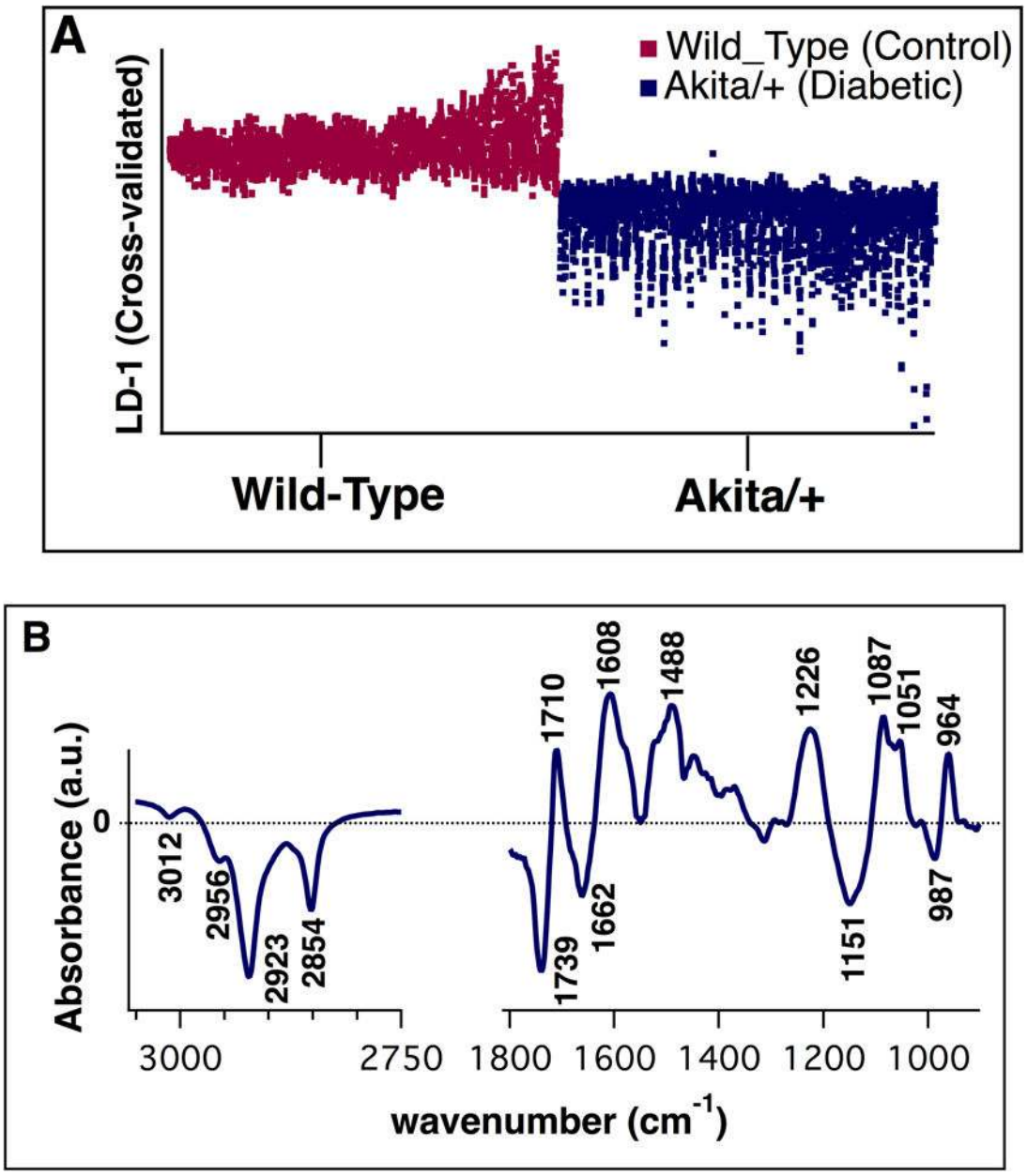

Figure 4.

comparison of the wt vs. akita/+ retina tissue generated from pca-lda analysis. a) 1-dimensional (1d) cross-validated scores plot of the spectra that revealed classification. b) corresponding cluster vector plot showing differentiating bands in the biomedical-ir spectral region (1800–900 cm^{-1}) and lipid region (3050–2750 cm^{-1}). spectra are generated from the whole tissue (all retinal layers) and 3600 spectra from each group of samples are used for comparison.

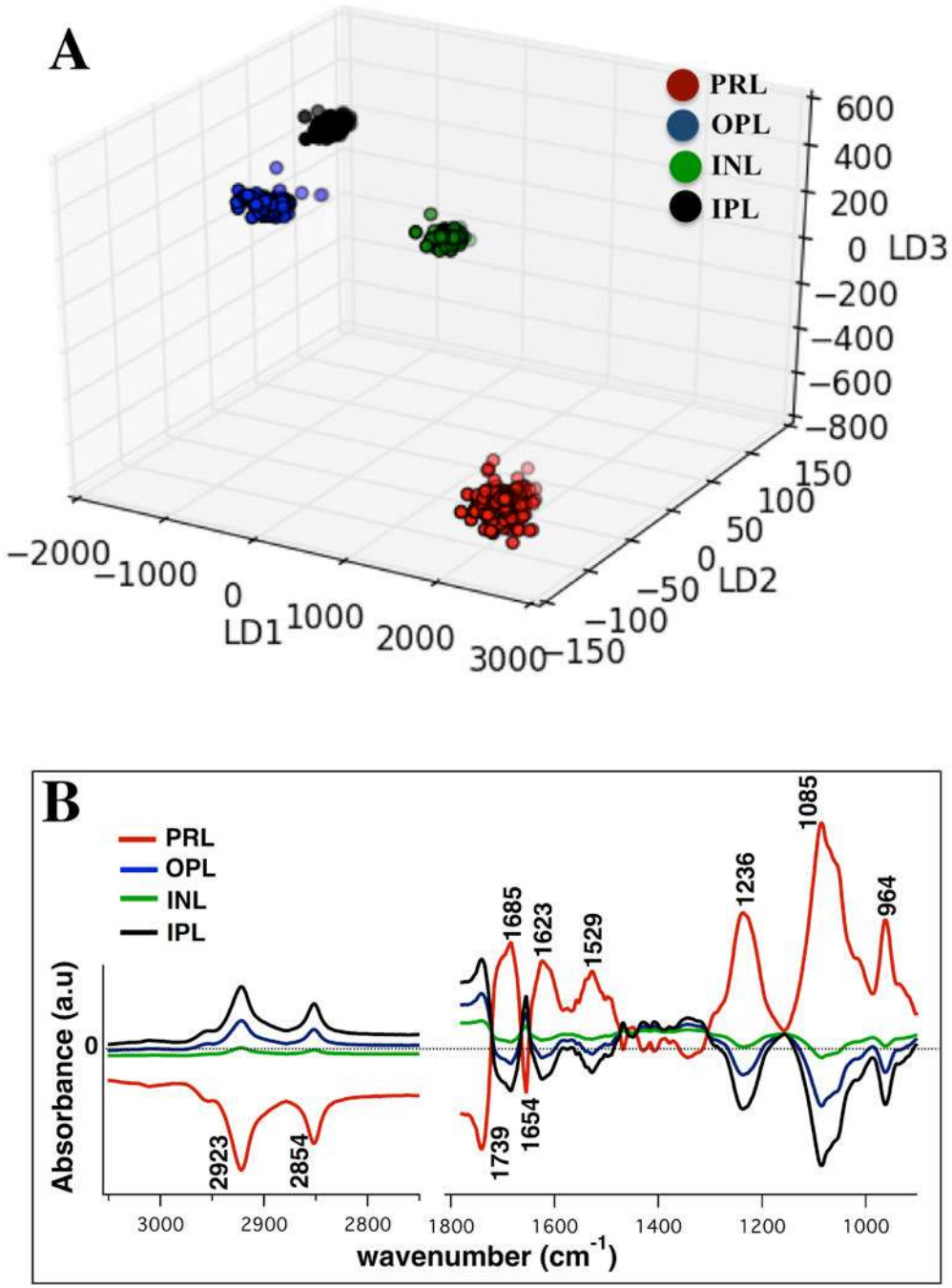

Figure 5.

comparison of the prl (red dots), opl (blue dots), inl (green dots) and ipl (black dots) of akita/+ retina tissue by means of pca-lda is shown. a) 3-dimensional (3d) scores plot of the spectra showing the separation of the prl from other layers along ld1. b) cluster vector plot of a; highlighting the discriminating wavenumbers responsible for the separation. nearly 1500 spectra from each layer of the retina were generated and compared.

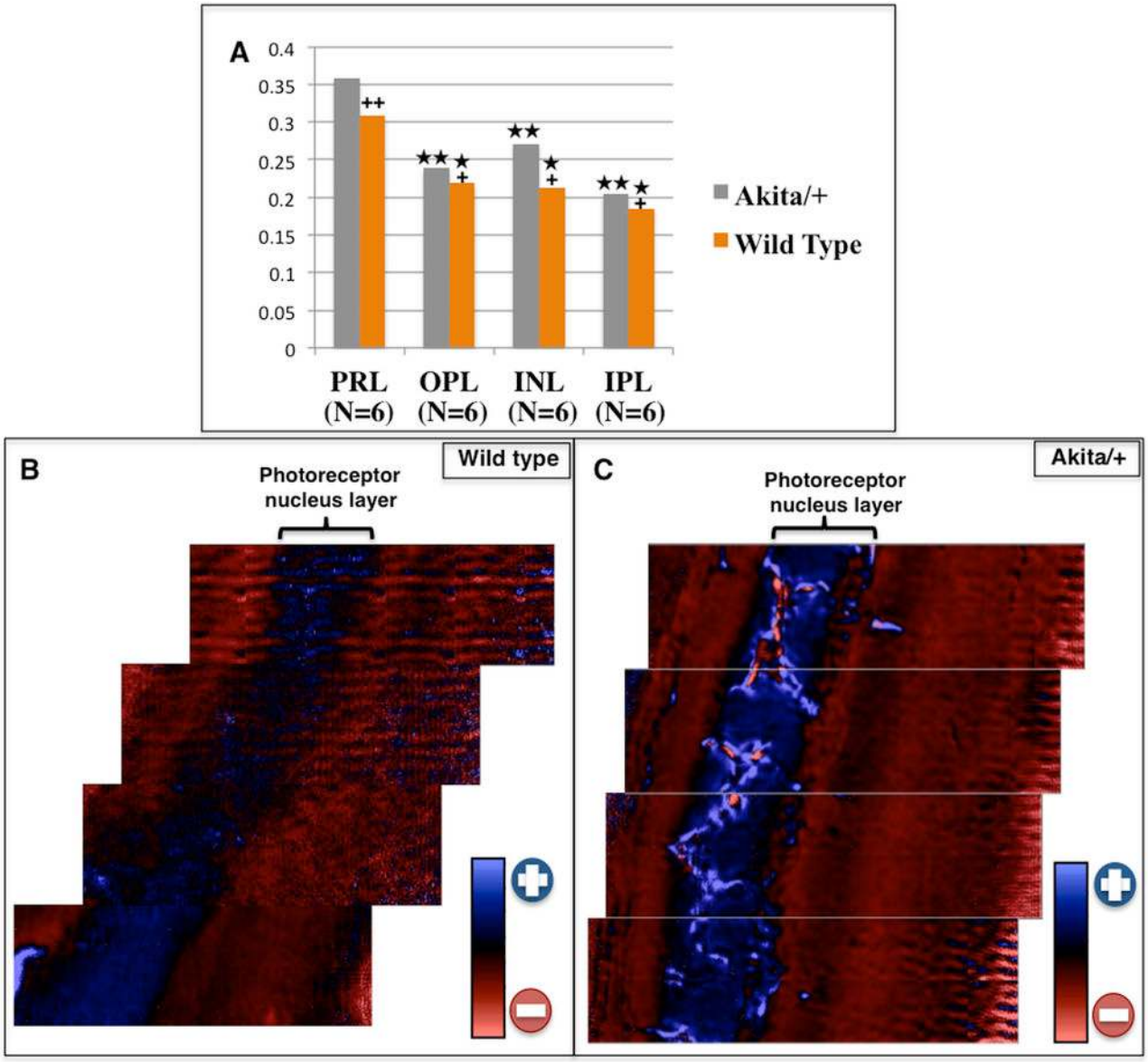

Figure 6.

the ratio of νasym po2- band to protein band for the wt and akita/+ retina tissues. a) comparison of the νasym po2-/protein (1230 cm^{-1}/amide ii (1546 cm^{-1})), and among the prl, opl, inl and ipl within each tissue. + was used for the comparison of the wt and the akita/+ and ★ was used for the comparison of the prl with the rest of the layers. $p< 0.05$ is the level of significance. b,c) spectral maps of the νasym po2-/protein ratio in wt (b) and akita/+ (c) tissues, showing the absorption strength of the prl among layers. the representative images are on a three-color coded color scale, where the blue/red color is associated with the highest/lowest absorption. the spectral regions 1180–1280 cm^{-1} (for the phosphate band) and 1500–1750 cm^{-1} (for protein band amide ii) were used as a baseline.

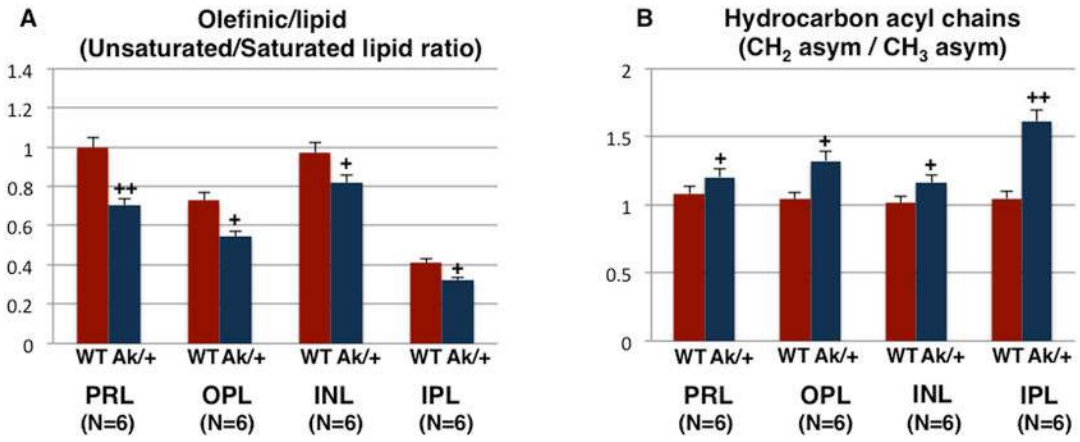

Figure 7.

bar graphs of the olefinic/lipid ratio and qualitative hydrocarbon acyl chains in lipids are shown. a) the unsaturated/saturated lipid ratio and b) the ch2/ch3 asym ratio of the wt and akita/+ retina tissues were compared. + was used for comparison of wt and akita/+ tissues.

Table 1

Band assignments for the retina tissue spectra[55–59]

Peak Frequency (cm^{-1})	Assignments
966	Symmetric PO_4^- stretching (DNA) and deoxyribose- phosphate skeletal motions
1010	C-O stretching; C-C stretching; DNA ribose
1051	C–O stretching: deoxyribose/ribose DNA, RNA/glycogen
1087	Symmetric stretching of PO_2^-:phospholipids and nucleic acids
1150	C-O, C-C stretching, C-O-H, C-O-C deformation of carbohydrates/glycogen
1172	CO-O-C asymmetric stretching: ester bonds in cholesterol esters
1240	Asymmetric stretching of PO_2^-:phospholipids and nucleic acids
1388	Symmetric CH_3 bending lipids, proteins, and nucleic acids
1546	Amide II- α helical structure of proteins (mainly N-H bending and C-N stretching)
1637	Amide I- β sheets
1656	Amide I- α helical or unordered structure of proteins (proteins C-O stretching, C-N stretch, CCN deformation)
1681	Amide I- β sheets, antiparallel/random coil (mainly C-O stretching)
1712	Base pair carbonyl (C=O), nucleic acids, DNA, RNA, oxidation of cellular lipids, short chain aldehyde
1741	C=O stretching: ester in phospholipids
2850	Symmetric stretching of CH_2; lipids
2873	Symmetric stretching of CH_3; lipids
2921	Asymmetric stretching of CH_2; lipids
2960	Asymmetric stretching of CH_3; lipids
3012	Olefinic=C-H stretching; unsaturated fatty acids

Table 2

Major wavenumbers responsible for the discrimination between WT and Akita/+ retinal tissue (including all retinal layers)[55–59]

Peak Frequency (cm^{-1})	Assignments
3012	Olefinic=C-H stretching; unsaturated fatty acids
2956	Asymmetric stretching of CH_3; lipids
2923	Asymmetric stretching of CH_2; lipids
2854	Symmetric stretching of CH_2; lipids
1739	C=O stretching: ester in phospholipids
1710	Base pair carbonyl (C=O), nucleic acids, DNA, RNA, oxidation of cellular lipids, fatty acids
1662	Amide I- turns 3_{10} helical structure of proteins (mainly C-O stretching; contribution from C-N stretching)
1550	Amide II (N-H bending; C-N stretching)
1488	Deformation C-H
1226	Asymmetric stretching of PO_2^-:phospholipids and nucleic acids
1151	C-O, C-C stretching, C-O-H, C-O-C deformation of carbohydrates/glycogen
1085	Symmetric stretching of PO_2^-:phospholipids and nucleic acids
1051	C–O stretching: deoxyribose/ribose DNA, RNA/nucleic acids
987	Nucleic acids and proteins; protein phosphorylation
964	Nucleic acids, Symmetric PO_4^- stretching (DNA) and deoxyribose; phosphate skeletal motions

Table 3

Major wavenumbers responsible for the discrimination between distinctive diabetic retinal layers (PRL, OPL, INL, and IPL)[55–59]

Peak Frequency (cm^{-1})	Assignments
2921	Asymmetric stretching of CH_2; lipids
2850	Symmetric stretching of CH_2; lipids
1739	C=O stretching: ester in phospholipids
1685	Amide I- β sheets, antiparallel/random coil (mainly C-O stretching, contribution from C-N stretching)
1654	Amide I- α helical or unordered structure of proteins (proteins C-O stretching, C-N stretch, CCN deformation)
1623	Amide I of aggregated strand structures (mainly C-O stretching, contribution from C-N stretching)
1529	Amide II- β sheets (mainly N-H bending and C-N stretching)
1236	Asymmetric stretching of PO_2^-:phospholipids and nucleic acids
1085	Symmetric stretching of PO_2^-:phospholipids and nucleic acids
964	Nucleic acids, Symmetric PO_4^- stretching (DNA) and deoxyribose; phosphate skeletal motions